

Characterisation of Geometric Fidelity as a Function of Attenuation in Tomographic Volumetric Additive Manufacturing

N. Pellizzon*, J. Spangenberg*

*Department of Civil and Mechanical Engineering, Technical University of Denmark,
Kongens Lyngby, 2800, Denmark

Abstract

In tomographic volumetric additive manufacturing, 2D intensity-modulated image-sets are generated using the Radon transform. These images are shone across liquid photopolymer forming a layerless 3D target object fashion as a physical realisation of the adjoint to the Radon transform: the back-projection. However, use of the exponential Radon transform back-projection to account for energy losses incurred from light attenuation has been mostly overlooked in literature. The resulting deviation between print and target depends on the photopolymer's attenuation coefficient and the distance over which the images are shone. In this novel numerical study, geometry fidelity is interrogated for multiple attenuation levels suggesting a threshold above which this effect should be included in image-set optimisation to account for real-world physics. During generation of the image-sets, each optimisation iteration compares the current image-set reconstruction to the target geometry to calculate the error. Thus considering attenuation increases the veracity of this error, theoretically resulting in a better print.

Introduction

Volumetric Additive Manufacturing (VAM) is a new family of Additive Manufacturing (AM) methods that produces parts in a layerless fashion. The most popular of the VAM methods is Tomographic VAM (TVAM), invented by Kelly *et al.* [1], and draws heavily on the concepts of tomographic reconstruction from the field of Computed Tomography (CT). Typical use cases of CT, such as MRI or (μ -) CT imaging, involve taking 2D images while navigating a target object and then digitally reconstructing this image-set into a 3D representation. TVAM inverts the physical and digital steps by creating the sequence of 2D images digitally which are then shone into a rotating vial of liquid photopolymer. Since a single image delivers insufficient energy to surpass the threshold energy dose to cure the photopolymer, the rotation of the print vial coupled with the changing images enables a 3D accumulation of light energy to develop over the course of a rotation, or multiple rotations. Thus, the curing reaction is delayed until the completion of at least one full rotation stage which enables the layerless characteristic of TVAM. This defining feature of TVAM results in prints with isotropic material properties, improved surface finish permitting objects such as optical lenses to be printed [2], and simplified overprinting from the one-step process [1, 3].

However, generating images that once shone can cause energy accumulation in the same shape as the target object is challenging. Images representing a target object are created with the Radon transform, and in digital reconstruction, its adjoint the Filtered Back Projection (FBP) is used

to reconstruct and recover the target. The Ram-Lak filter, a common choice for FBP, introduces negative values into the image. This is no obstacle in the digital world where it is possible to “shine” negative light, however, in the physical world this is simply impossible. Thus, the image-sets generated by FBP must be further adjusted and subsequently optimised to suit the physical limitations of TVAM. Many image-set optimisation algorithms exist such as the original Computed Axial Lithography (CAL) algorithm [1], the popular Object-Space Model Optimisation (OSMO) [4], an algorithm using test prints in a closed-loop feedback system [5], and 3D ray-tracing [6].

A further challenge to physically shining the image-set is the attenuation of the light rays as they pass through the photopolymer. In the work by Rackson *et al.* [4] attenuation is incorporated in their OSMO algorithm by using a ray tracing projection method. Chen *et al.* [7] incorporated attenuation in the form of an attenuation matrix as the discretised form of the associated exponential Radon transform (the backward Radon transform operation) into their maximum likelihood-expectation maximisation algorithm which in later work is used to produce prints using high-attenuation photopolymers [8].

However, despite the notice given to attenuation, it is not yet clear how deleterious its effects can be on the fidelity of the reconstruction and how this changes with attenuation severity. This paper infers a numerical-based critical attenuation level using Jaccard similarity to measure geometric fidelity. Further, this work investigates the improvement in Jaccard similarity from including attenuation effects via a discretised form of the associated exponential Radon transform in-the-loop of the foundational CAL optimisation algorithm.

Methodology

Reconstruction of a target image $f(\mathbf{r}) = f(x, y)$ is achieved via the back projection T^* . This requires the image-set $g(\mathbf{r}, \mathbf{j})$ which is composed of a set of line integrals of $f(\mathbf{r})$ over the line l with direction vector $\mathbf{j} = (\cos(\theta), \sin(\theta))$ and parametrised by (p, θ) , as defined and illustrated in Figure 1a. In the ordinary case, attenuation is not considered, and a back projection

$$f(\mathbf{r}) = T^*[g](\mathbf{r}) = \int_0^{2\pi} g(\mathbf{r} \cdot \mathbf{j}) d\theta \quad (1)$$

simply smears the projected light source values across the domain summing for each angle-image pair. The Associated Exponential Radon Transform (AERT) T_μ^* introduces a decay term yielding an attenuated back projection and can account for the decay in light energy as it gets absorbed by the photopolymer [1, 4, 7–9]. The AERT is illustrated in Figure 1c, and is defined by Tretiak and Metz [10] as

$$f(\mathbf{r}) = T_\mu^*[g](\mathbf{r}) = \int_0^{2\pi} g(\mathbf{r} \cdot \mathbf{j}) e^{\mu \mathbf{r} \cdot \mathbf{k}} d\theta \quad (2)$$

where $\mathbf{k} = (-\sin(\theta), \cos(\theta))$ as the orthogonal direction vector to \mathbf{j} is aligned with the light ray being back-projected and μ is the absorption coefficient such that when $\mu = 0$, the non-attenuated back-projection (1) is recovered. A comparison of these back projections is shown in Figures 1b and 1c.

As the exponential decay term in the integral of Equation 2 has an upper bound of 1, it can be implemented across the projection width as an attenuation matrix which is then multiplied with each single back-projection for a given θ [7, 8]. The attenuation matrix must additionally

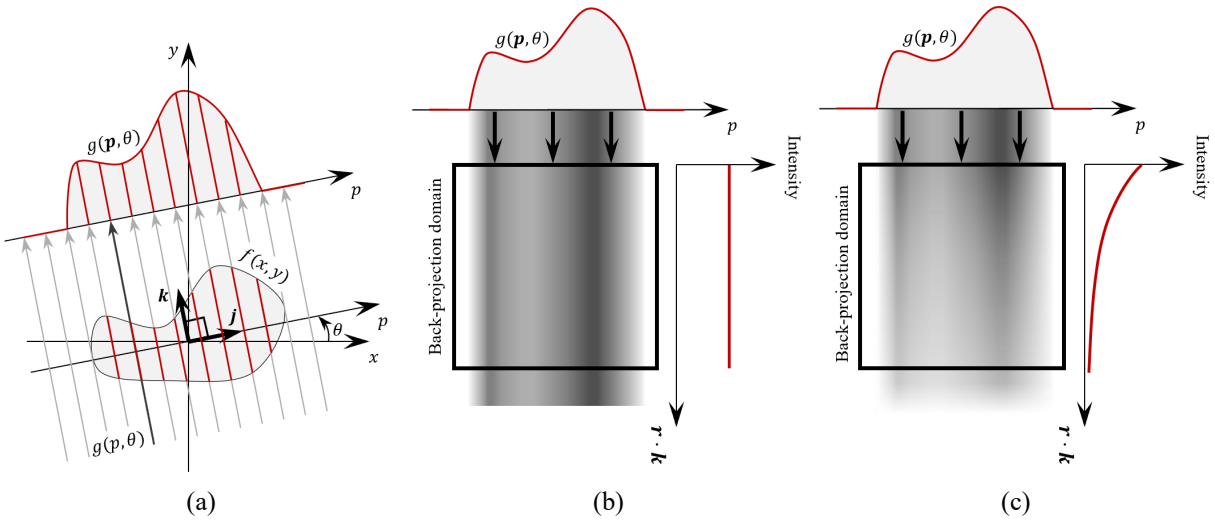


Figure 1: Diagrammatic overview of tomographic reconstruction. (a) The Radon transform which maps image $f(x, y)$ to $g(\mathbf{p}, \theta)$. (b) Back-projection at angle θ . (c) Attenuated back-projection at angle θ .

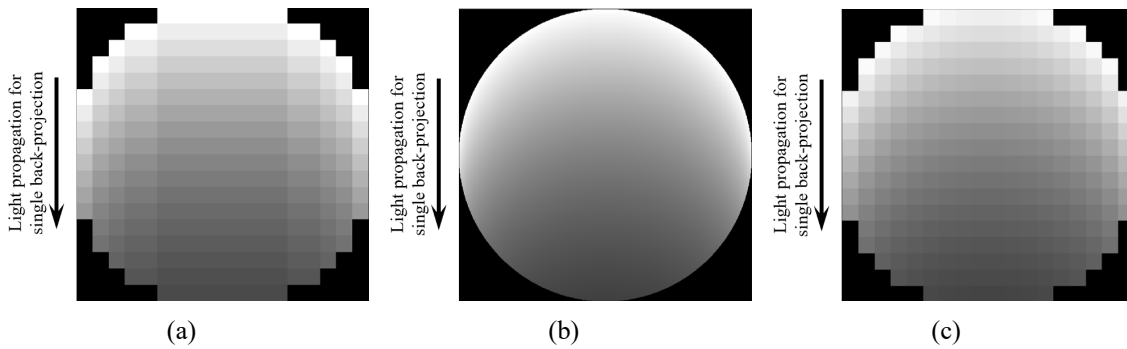


Figure 2: Attenuated back projections masked by a circular/cylindrical printing volume. Note how unlike in Figure 1b, attenuation begins at the perimeter of the circular mask as the back-projection domain takes on the circular shape. (a) A 20×20 sized attenuation matrix showing a vertical stripe down the centre due to the poor perimeter smoothness of the discretised circular printing region. (b) A 1000×1000 sized attenuation matrix has a much smoother circular perimeter and therefore the stripe artifact is minimised. (c) The 1000×1000 sized attenuation matrix interpolated onto a 20×20 sized grid; the small matrix size is retained without the stripe artifact.

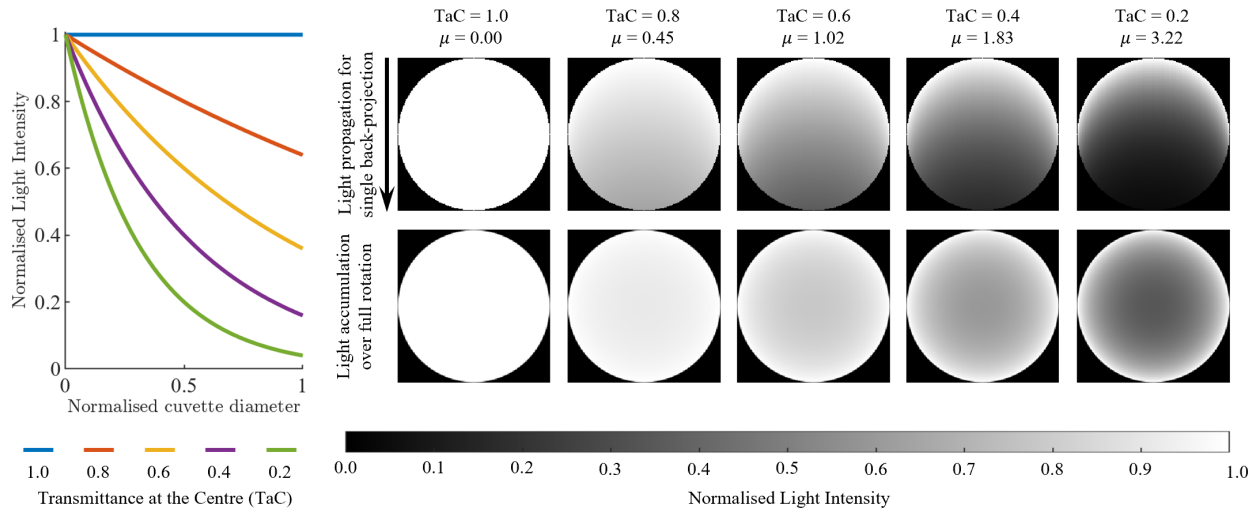


Figure 3: Five light energy decay profiles (*left*). The decay across the printing vial for a fully illuminated image is shown for the profiles (*top row, right*) with a light propagation direction of top to bottom and the ensuing reconstruction from 360 projections is also shown (*bottom row, right*).

contain the geometric correction to account for the circular region of interest (in a 2D case) which forms the printing cuvette; since there is no photoinitiator outside of the print volume to attenuate the light rays.

However, care must be taken in defining the attenuation matrix as, in Cartesian coordinates, a coarsely discretised circle leads to artificially uniform regions at the cardinal points. For example, in Figure 2a, the central North-South region has uniform attenuation stripe in the coarsely discretised domain. As the pixel count increases and the circle boundary smoothness is recovered, this effect lessens and curved attenuation propagation front is achieved (Figure 2b). Since the attenuation matrix need only be calculated once (as it may be simply rotated by the angle θ of the back-projection), it is thus advantageous to calculate the attenuation matrix on a very fine grid which can then be reduced whilst retaining the better attenuation representation, as in Figure 2c.

Transmittance at the centre

Loss of light energy across the printing domain can be caused by either a high μ or by the size of the printing vial being significantly large enough such that even a small non-zero μ will result in significant energy loss over the projection length. To this end, Chen *et al.* [8] coined the term Transmittance at the Centre (TaC)

$$\text{TaC} = e^{-\mu r} \quad (3)$$

to represent attenuation such that it is not explicitly defined in terms of material property μ or printer geometry r which is the radius of the cuvette of photopolymer. Intuitively, TaC represents the fraction of light present in the centre of the print vial with respect to the incident light. As such, reconstruction quality may be compared for a range of materials or print vial sizes with the same TaC.

Five light energy decay profiles are illustrated in Figure 3 for $\text{TaC} \in [1.0, 0.8, 0.6, 0.4, 0.2]$.

For each decay profile, the attenuation matrix is shown (top row) considering a unit valued projection image $g(\mathbf{r} \cdot \mathbf{j}) = \mathbf{1}$. These images are equal to a single-angle (e.g. $\theta = 0$) back-projection. The bottom row shows the light accumulation (or reconstruction) over the full rotation $\theta \in [0, 360)$ of this uniform projection image and serves as a reference for the worst-scenario effects of attenuation on the brightest achievable projection image set. Typical TaC values range from 0.70 – 0.95 [1, 9] but experimental results with TaCs as low as 0.10 have been shown to showcase novel image-set optimisation algorithms [8].

Numerical setup

Baseline projections are generated using the unmodified CAL image-set optimisation algorithm [1] with a threshold of 0.8 and default parameters and with no adjustments made to the publicly available MATLAB code [1]. In the optimisation of the projection image-sets, at each iteration the current reconstruction is compared to the target to ascertain the error and thus determine how the projection image-set should be adjusted in the next iteration. Therefore, it is at this point that the attenuation matrix is applied to create attenuation-aware projections. This adjustment to the image-set generation algorithm thus includes some of the physical reality of the printing process.

The target geometry used throughout is Rodin’s *The Thinker* statue. A sample of 2D slices is chosen to give a selection through the part and to also highlight diverse geometries. This makes use of the common parallel-beam projection geometry used in TVAM [1, 11] that means 2D horizontal slices can be treated independently.

Geometric fidelity of both attenuated and non-attenuated reconstructions is measured with the Jaccard similarity index, which for two sets A and B is

$$J(A, B) = \frac{|A \cap B|}{|A \cup B|}. \quad (4)$$

Separating a reconstruction into in-part and out-of-part regions to compare the printed geometry to the target geometry requires determining an energy threshold (here analagous to the light intensity received). Above the threshold value, the polymer is considered cured and thus that voxel part of the printed result, and below it, the polymer is considered uncured and still liquid. The Jaccard similarity index then compares the target in-part region (A) with the reconstructed demarcated in-part region (B), or the complement target out-of-part region with the reconstructed out-of-part region.

Results and Discussion

The effect of attenuation on reconstruction quality

A projection image-set is generated with CAL and reconstructed at five TaC levels ranging from the non-attenuating TaC = 1.0 for which CAL is designed for, down to TaC = 0.2 where only 20% of incident light intensity is measured at the centre of the printing vial.

As expected, the geometric fidelity of the reconstruction decreases with TaC. The $x - y$ slices in Figure 4 showcase: a large, roughly spherical shape in the lower slice taken through the rock; a highly convex geometry in the middle slice taken through the seat of the model; and the

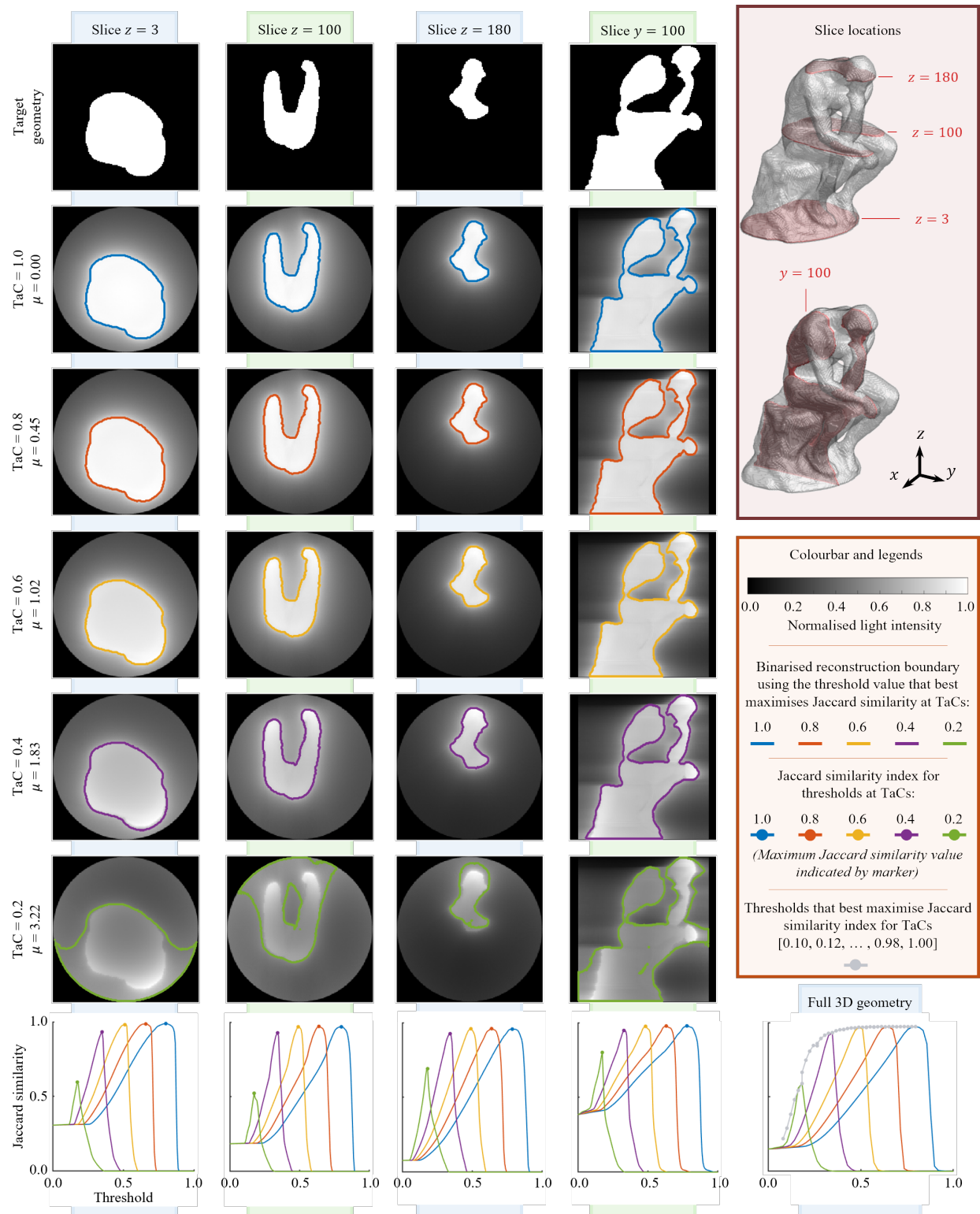


Figure 4: A set of projection images is back-projected across varying attenuation levels. The normalised images show the resulting reconstructions. Boundaries demarcating in-part and out-of-part that give the best Jaccard similarity for $TaC = [1.0, 0.8, 0.6, 0.4, 0.2]$ are overlaid. The progression of the Jaccard similarity with respect to the thresholds that demarcate the limits is shown for each slice and the full geometry where a finer stencil of thresholds is shown in grey.

smaller, off-centre upper slice with a complex meandering perimeter taken through the shoulders. For all these slices, lower light intensity levels in the centre of the printing vial due to attenuation are most evident in the bottom row ($TaC = 0.2$) where the decay gradient from vial perimeter to centre is clearly seen. In the vertical $y - z$ slice, this translates to light decaying from the vertical edges of the cylindrical printing vial towards the vertical axial line. A large range of intensity values in the in-part region is undesirable, due to it leading to a non-homogeneous curing degree in less powerful printing systems requiring multiple revolutions to deliver sufficient energy to cause the solidification reaction. Additionally, due to the wider the in-part intensity range, it is more likely that curing will take place over multiple revolutions, which can lead to problems like sedimentation where a cured and denser region begins to sink in the surrounding liquid polymer and consequently the regions that cure in later revolutions forming in the relative incorrect locations, or the overcuring of regions that form first.

A range of thresholds $t \in [0, 1]$ is used to segment the reconstruction into in-part and out-of-part regions for Jaccard similarity evaluation. These are plotted across the bottom row in Figure 4. The maximum Jaccard similarity value achievable for any of the TaC cases is indicated by the marker. The in-part to out-of-part partition line from the corresponding threshold is overlaid on the reconstructions.

The CAL projection image-set performs well for $TaC = 1.0$ where a threshold of 0.8 (given as a parameter to the algorithm) produces the highest Jaccard similarity across these results. Further, for $TaC = [0.8, 0.6, 0.4]$, the Jaccard similarity does not suffer provided a decrease in threshold is permitted with the Jaccard similarity is still above 0.9. The only poorly performing case is $TaC = 0.2$ with a significant drop in Jaccard similarity which is visually most apparent in the reconstruction boundaries in the $x - y$ slices that clearly enlarge the in-part area.

Looking at the relationship between Jaccard similarity and threshold calculated on the full 3D reconstruction, the trend of sharp decrease in Jaccard score from $TaC = 0.4$ to $TaC = 0.2$ persists throughout the part. The plot in the bottom right of Figure 4 which illustrates this also contains the trend curve of the best Jaccard values for a finer stencil of TaC values. This curve supports the statement that, for this geometry, there is a significant reduction of achievable geometric fidelity for $TaC < 0.4$ if projections generated with no attenuation awareness are used for printing.

Attenuation in-the-loop: how this improves high-attenuation printing

Projections are generated using a modified CAL code with the addition of the attenuation calculation. The design point of $TaC = 0.2$ chosen based on the results from the previous subsection that showed a significant reduction in achievable geometric fidelity occurred for $TaC < 0.4$.

Compared to the unmodified reconstruction at $TaC = 0.2$ shown in Figure 4 that does not consider attenuation when generating the projection image-set, the new $TaC = 0.2$ reconstruction in Figure 5 has a smaller range of intensity values in the in-part region. This is shown by the greater homogeneity of intensity of the in-part region. However, the threshold values that achieve these maximum Jaccard scores have decreased. This is somewhat deceptive as whilst there does exist a “real-life” energy dose threshold for the photopolymer to cure, provided the range of light intensity

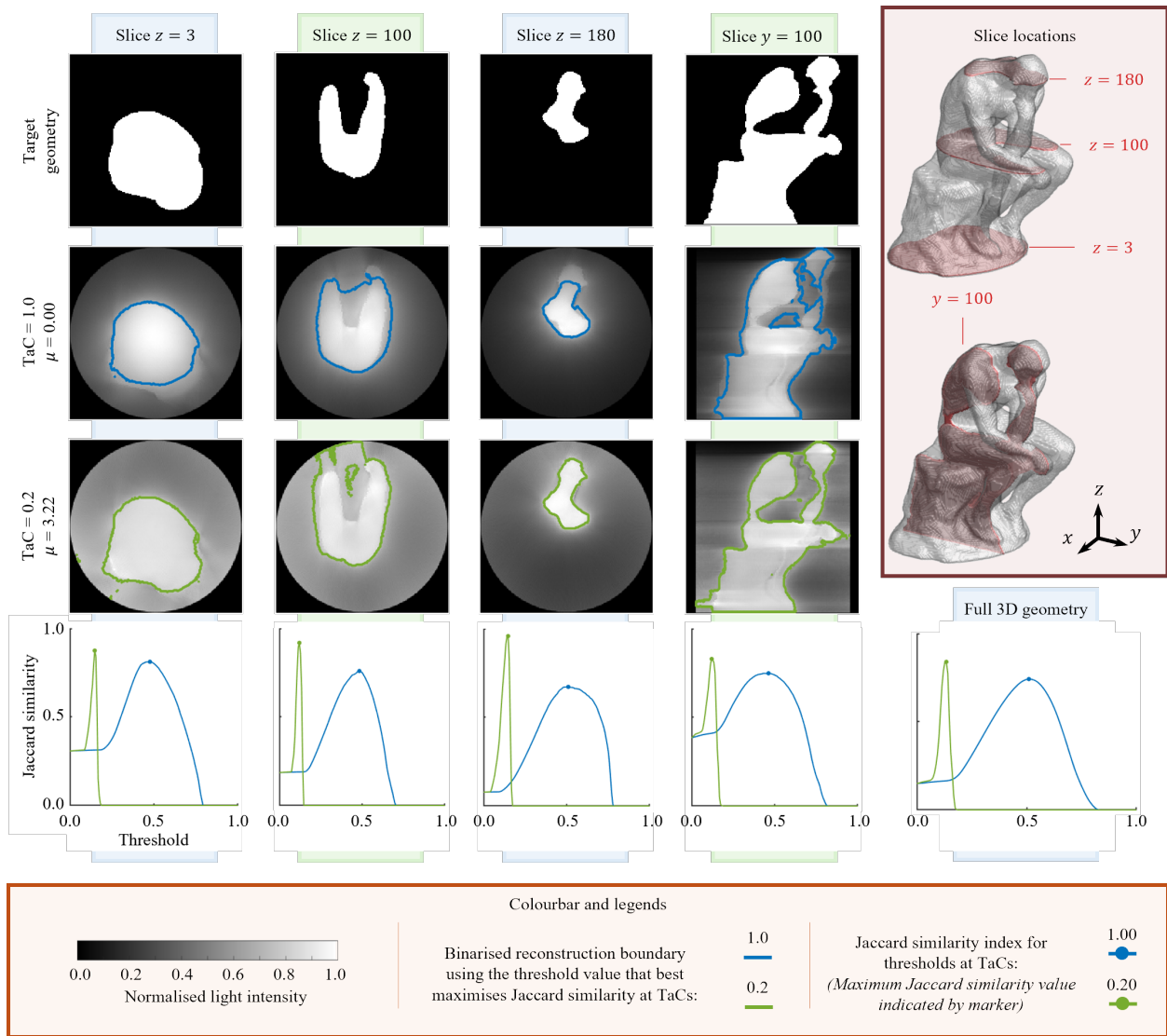


Figure 5: A set of attenuation-aware projection images generated for the $TaC = 0.2$ design point are back-projected with no attenuation and design point attenuation. Boundaries demarcating in-part and out-of-part that give the best Jaccard similarity for the two different TaC values are overlaid. The progression of the Jaccard similarity with respect to the thresholds that demarcate the limits is shown for each slice and the full geometry where a finer stencil of thresholds is shown in grey.

values is small, the reconstructions can simply be normalised as they are shown in Figure 5 thus scaling the threshold with the reconstruction.

Turning to Jaccard similarity, for the reconstructions from the attenuation-aware projections the higher Jaccard score is now achieved by the lower $TaC = 0.2$ case. Quantitatively, there is a noticeable improvement for the new $TaC = 0.2$ reconstruction where the Jaccard similarity score rises from approximately 0.6 to over 0.8 for the full geometry. This supports the use of a design point TaC to create an attenuation matrix to use in the generation of projection image-sets to improve reconstruction (and print) accuracy in cases where unmodified CAL will not suffice.

Conclusions

In Tomographic Volumetric Additive Manufacturing (TVAM), attenuation of the projected image-sets across the printing domain can pose a significant threat to the geometric fidelity of the printed part. For the geometry used in this work, it is shown that the Jaccard similarity index drops significantly when light attenuates more than 60% over the radius of the printing vial. When there is no attenuation, using CAL projection image-sets, the maximum Jaccard similarity achievable is over 0.95. This drops to below 0.6 when light attenuates by 80% of incident value over the printing vial radius.

By augmenting the existing CAL code so that interim iteration reconstructions are attenuated and then compared to the desired target geometry (rather than comparing the unattenuated reconstruction to the target) the Jaccard similarity can be increased. For the case when light attenuates by 80% of incident value over the printing vial radius, this single adjustment to CAL increased the Jaccard from approximately 0.6 to 0.8.

Further investigation into other geometries is now paramount to distinguish if a universal attenuation limit can be identified and applied broadly to any geometry. This would be greatly supported by experimental validation using a variable attenuation system. Nonetheless, it is clear that attenuation-aware generation of projection image sets is vital and beneficial for improving geometric fidelity in high attenuation TVAM systems.

Acknowledgements

The authors would like to acknowledge the support of the Independent Research Fund Denmark (Contract No. 0171-00115B). NP thanks the Thomas B. Thriges Fond for their support through a travel grant.

References

- [1] B. E. Kelly, I. Bhattacharya, H. Heidari, M. Shusteff, C. M. Spadaccini, H. K. Taylor, Volumetric additive manufacturing via tomographic reconstruction, *Science* 363 (6431) (2019) 1075–1079. doi:10.1126/science.aau7114.
- [2] D. Webber, Y. Zhang, K. L. Sampson, M. Picard, T. Lacelle, C. Paquet, J. Boisvert, A. Orth, Micro-optics fabrication using blurred tomography, *Optica* 11 (5) (2024) 665–672. doi:10.1364/OPTICA.519278.
- [3] C. Darkes-Burkey, R. F. Shepherd, Volumetric 3d printing of endoskeletal soft robots, *Advanced Materials* 36 (33) (2025) 2402217. doi:10.1002/adma.202402217.
- [4] C. M. Rackson, K. M. Champley, J. T. Toombs, E. J. Fong, V. Bansal, H. K. Taylor, M. Shusteff, R. R. McLeod, Object-space optimization of tomographic reconstructions for additive manufacturing, *Additive Manufacturing* 48 (2021) 102367. doi:10.1016/j.adma.2021.102367.
- [5] D. Loterie, P. Delrot, C. Moser, High-resolution tomographic volumetric additive manufacturing, *Nature Communications* 11 (1) (2020) 852. doi:10.1038/s41467-020-14630-4.

- [6] D. Webber, Y. Zhang, M. Picard, J. Boisvert, C. Paquet, A. Orth, Versatile volumetric additive manufacturing with 3D ray tracing, *Optics Express* 31 (4) (2023) 5531–5546. doi:10.1364/OE.481318.
- [7] T. Chen, H. Li, X. Liu, Statistical iterative pattern generation in volumetric additive manufacturing based on ML-EM, *Optics Communications* 537 (2023) 129448. doi:10.1016/j.optcom.2023.129448.
- [8] T. Chen, S. You, L. Xu, C. Cao, H. Li, C. Kuang, X. Liu, High-fidelity tomographic additive manufacturing for large-volume and high-attenuation situations using expectation maximization algorithm, *Additive Manufacturing* 80 (2024) 103968. doi:10.1016/j.addma.2024.103968.
- [9] I. Bhattacharya, J. Toombs, H. Taylor, High fidelity volumetric additive manufacturing, *Additive Manufacturing* 47 (2021) 102299. doi:10.1016/j.addma.2021.102299.
- [10] O. Tretiak, C. Metz, The exponential radon transform, *SIAM Journal on Applied Mathematics* 39 (2) (1980) 341–354. doi:10.1137/0139029.
- [11] S. Tisato, G. Vera, A. Mani, T. Chase, D. Helmer, An easy-to-build, accessible volumetric 3d printer based on a liquid crystal display for rapid resin development, *Additive Manufacturing* 87 (2024) 104232. doi:10.1016/j.addma.2024.104232.